

Distributions of pore sizes and atomic densities in binary glasses revealed by molecular dynamics simulations

Maxim A. Makeev¹ and Nikolai V. Priezjev²

¹*Department of Chemistry, University of Missouri-Columbia, Columbia, MO 65211 and*

²*Department of Mechanical and Materials Engineering,*

Wright State University, Dayton, OH 45435

(September 19, 2021)

Abstract

We report on the results of a molecular dynamics simulation study of binodal glassy systems, formed in the process of isochoric rapid quenching from a high-temperature fluid phase. The transition to vitreous state occurs due to concurrent spinodal decomposition and solidification of the matter. The study is focused on topographies of the porous solid structures and their dependence on temperature and average density. To quantify the pore-size distributions, we put forth a scaling relation that provides a robust data collapse in systems with high porosity. We also find that the local density of glassy phases is broadly distributed, and, with increasing average glass density, a distinct peak in the local density distribution is displaced toward higher values.

PACS numbers: 34.20.Cf, 68.35.Ct, 68.35.Np

I. INTRODUCTION

The glass transition is generally envisaged as a dynamic transition from a thermodynamically equilibrium liquid state to a non-equilibrium (glassy) state [1–3]. The transition occurs in atomic, molecular, and polymeric liquids (as well as in a wide variety of other forms of matter), under the condition of rapid decrease in temperature; that is, cooling of the liquid phase must be fast enough in order to avoid material crystallization [2, 3]. Despite a long history of studies aimed at understanding the vitreous state of matter, the phenomenon of glass transition still remains to be one of the most intriguing unsolved problems in condensed matter theory [4, 5]. In the light of overwhelming complexity of the glass problem, atomistic simulations of judiciously chosen model systems can be of great assistance in gaining a more elaborate understanding of various structural and dynamical aspects pertained to glassy materials. One of the most successful atomistic models, developed to date, is the Kob-Andersen (KA) binary mixture model [6]. Atomic simulations, performed using the KA model, cover a wide range of topics and include - but not limited to - the simulation studies of Refs. [7–13]. The KA model have been proven useful for gaining insight into topics ranging from atomic-level structure of glasses to longer-range dynamical correlation. Also, it was instrumental in revealing the existence of spatio-temporal correlations in dynamical behavior of glassy materials (i.e., dynamic heterogeneity [14, 15]).

There exist a number of approaches to describe the glass transition phenomenon. A somewhat simplified approach is based upon the concept of free volume. Originally, the concept was introduced to describe the glass transition in polymeric systems in Ref. [16]. The analytical representation of free volume was later formulated by Doolittle [17]. Within the framework, developed in Ref. [18], the glass transition occurs as a result of decrease in free volume of the amorphous phase below a certain value. This makes a possibility of an isochoric glass transition in a glass-forming system seemingly counterintuitive, as volume per atom in such system must decrease in a vicinity of the transition. A possible explanation of vitrification at constant volume is that the glass transition is accompanied by spinodal decomposition [19–24]. Correspondingly, the separation of the liquid phase into solid and void phases occurs; the process of transition to a glassy phase is thus dynamically concurrent with that of spinodal decomposition. The non-equilibrium phenomenon of phase separation has been studied extensively in binary mixtures *via* both theoretical (Monte Carlo

simulations) and experimental means [25]. Within the mean-field theory framework [26], the initial instability is defined by negative chemical potential derivative with respect to concentration in binary mixtures, and by negative pressure derivative with respect to the local density in one-component fluids. On the other hand, only a few computational studies of phenomena taking place during rapid quenching of liquids below the glass transition at a constant volume have been performed in the past.

A classical molecular-dynamics simulation study of an isochoric vitrification in model two-dimensional Lennard-Jones (LJ) binary mixtures was reported in Ref. [27]; model polymeric systems were treated by a similar computational approach in Ref. [28]. Significant theoretical progress has been achieved in Ref. [29], where the glass transition was studied in model systems comprised of liquid phase droplets of small volume fraction, immersed in the glassy phase. The authors reported on a novel mechanism of the dynamics of coarsening, which was found to be driven by migration and eventual coalescence of liquid droplets in the glassy phase. More recently, dynamics of the spinodal decomposition in binary LJ mixtures, leading to vitrification, was investigated in Refs. [30, 31]. Among many other findings, the studies have provided important information on scaling relations, underlying the temporal evolution of binodal systems during a transition to a glassy state and reported on the effects of simulation system size on the corresponding scaling behaviors.

To date, several experimental studies have been performed to understand the constant volume vitrification [32–39]. The works include experimental studies of glass transition taking place in confined environments. In Refs. [33, 34], it was found that an isochoric vitrification under nanometer-scale confinement is realized in a close vicinity of the transition. More recent studies have provided a rather convincing experimental evidence that the glass transition in confined environments is an isochoric process [38, 39]. The major focus of these studies was centered on the issues related to dynamics of isochoric transition to glassy state. In the present study, the dynamical aspects are left beyond the scope. Rather, we concentrate on the micro-structural as well as topographical properties of the vitreous phases and make an attempt to bridge two extreme cases of free volume distributions; the ones that are characteristic for highly porous and dense glasses. Correspondingly, we consider systems, where, at the upper bound, the free volume is the largest one can achieve under the condition that the quenched samples are solid. At the lower bound, the free volume is

close to the one characteristic for conventional vitreous systems. Note that local regions in bulk glasses, where the free volume differs from the average, can be regarded as structural defects. Our approach provides interesting insights and connections to experimental studies of bulk glasses.

The remainder of the paper is organized as follows. The *modus operandi*, employed in this work, is described in the next section (Sect. II). In Sect. III, we present our simulation results on the topography of porous glasses and temperature dependence of the pore-size distributions. Also, we discuss the local density distributions in the solid phases. Finally, in Sect. IV, we summarize our principal findings and draw conclusions.

II. MODUS OPERANDI

In this work, the atomic systems are modeled as the KA binary (80:20) mixture of particles [6, 40] in a periodic box. Within the KA model's framework, a pair of atoms $\alpha, \beta = \{A, B\}$ interact *via* the Lennard-Jones (LJ) potential of the form:

$$V_{\alpha\beta}(r) = 4\varepsilon_{\alpha\beta}[(\sigma_{\alpha\beta}/r)^{12} - (\sigma_{\alpha\beta}/r)^6]. \quad (1)$$

The parameters of the interatomic potential are set to $\varepsilon_{AA} = 1.0$, $\varepsilon_{AB} = 1.5$, $\varepsilon_{BB} = 0.5$, $\sigma_{AA} = 0.8$, $\sigma_{BB} = 0.88$, and $m_A = m_B$ [40]. The cutoff radius of the potential is fixed at $r_{c,\alpha\beta} = 2.5\sigma_{\alpha\beta}$. The units of length, mass, energy, and time are measured in $\sigma = \sigma_{AA}$, $m = m_A$, $\varepsilon = \varepsilon_{AA}$, and $\tau = \sigma\sqrt{m/\varepsilon}$. The equations of motion are integrated using the Verlet algorithm with the MD time step of 0.005τ [41], and the temperature was controlled by velocity rescaling. Note that this work adopts the simulation methodology from Refs. [30, 31] in what related to the dynamical evolution of the systems under consideration. Correspondingly, all the behavioral features pertained to the dynamics of the glass transition and the spinodal decomposition are equivalent to those reported on in the above references. The initial atomic configurations are prepared as follows. First, the systems of 3×10^5 atoms were thoroughly equilibrated at the temperature of $1.5\varepsilon/k_B$ during $3 \times 10^4\tau$ at a constant volume. Five independent samples were prepared at each density in the range $0.2 \leq \rho\sigma^3 \leq 1.0$. Thereby equilibrated systems were then quenched to low temperatures; that is, well below the glass transition temperature of $0.435\varepsilon/k_B$ [30, 31]. The temperature of the glassy phases was varied in the range from 0.02 to $0.20\varepsilon/k_B$, the increment being

$0.01 \varepsilon/k_B$. At each fixed temperature, the atomic systems were relaxed at the constant volume during the additional time interval of $10^4\tau$ to form porous structures. It was found that the final atomic configurations are stable and correspond to solid phases at different densities. Moreover, the mobility of atoms is suppressed; the atoms remain largely in their positions at the time scales accessible to molecular dynamics simulations. In Refs. [30, 31], the authors found that the system-size effects become negligible, when the number of atoms is no less than $\simeq 3 \times 10^5$. The choice of the system size, used in this work, is based upon this finding.

III. RESULTS

A. Notes on isochoric glass transition

As made explicit above, the transition to glassy state at constant volume occurs *via* concurrent spinodal decomposition into material and void domains, and solidification in the systems undergoing rapid quenching to a low-temperature state. In Fig. 1, we show the representative examples of the topographical patterns, obtained in our simulations study. The major goal is to illustrate the larger-scale patterns in the glassy samples. Two main factors in shaping topography of the porous systems can be identified as the average density and temperature of glassy phase. It was found that the topographical patterns vary significantly with $\rho\sigma^3$. The free volume forms primarily conglomerates of complex nanometer-sized shapes. Formation of nanometer-scale channels running across the entire sample also found to occur at low $\rho\sigma^3$. The channels possess distinctly different characteristic length-scales, as compared to having nanometer-scale (in all three dimensions) voids. Also noteworthy is the observation that, in the whole range of average density variation, the pores show no tendency to adopt even a quasi-spherical shape. This observation can be of essence for theoretical models, dealing with nano-porous continua. The deviations from sphericity can be interpreted as resulting from highly inhomogeneous and asymmetric tension in the systems. As mentioned above, the degree of porosity in this work was varied in a rather wide range. This allows for comparison of the present results with findings reported in previous studies. While the low-density (high porosity) systems have not been investigated in sufficient details to have a comparative basis with experimental works, highly dense systems have been

a focus of experimental studies, which makes a qualitative comparison feasible. Indeed, the simulation results of our study show that the free volume distribution at $\rho\sigma^3 = 0.9$ is that of a random quantity. This is consistent with the recent experimental results of Ref. [42], where it was shown that the quenched-in free volume in glasses is randomly distributed. Furthermore, the shape of the distribution at the above density is similar to the experimental results, obtained on the hole-radius density distribution in polycarbonate and polystyrene [43]. Further micro-structural studies are needed to elucidate the nature of the glassy phase in the binodal systems. A work in this direction is currently in progress.

Next, we turn attention to the process of the porous structure formation. In Ref. [38], the authors noted that “... molecular liquids confined in native nanopores form a glass at constant volume under negative pressure”. Furthermore, it was observed that, in the region of positive pressures, the pressure dependence of the glass transition temperature, T_g , can be fitted to the Andersson-Andresson relation [44]. The extrapolation of the fit to the region of negative pressures was shown to provide a rather accurate description of the experimentally observed T_g behavior. In our study, we also find that the transition to the porous phase is driven by negative pressure. In the past, a number of studies were devoted to the mechanism of void formation under negative pressure. Thus, cavitation in LJ model systems was studied in Ref. [45] using the Monte Carlo method. It was found that there exists a critical density at which the volume fraction of void vanishes, and this density coincides with the minimum in the pressure *versus* density curve for inherent structures (the Sastry curve) at a negative pressure. In a subsequent study of Ref. [46], the Sastry curves were used to show that the properties of glass-forming mixtures depend on softness of the interatomic potentials. In this respect, it should be noted that our study employs the interaction potential with fixed softness. Given all of the above, it is important to provide some insights into the details of pressure variation with temperature of the solid phase and as a function of $\rho\sigma^3$.

In Figure 2, pressure versus temperature dependencies are plotted for the model systems with different $\rho\sigma^3$. As follows from Fig. 2, the transition to vitreous states and dynamical evolution of the glassy systems take place under negative pressure, which relaxes in the process of phase separation. At very low densities (see $\rho\sigma^3 = 0.2$ in Fig. 2), the pressure is relatively small and its absolute value is an increasing function of temperature when $T \lesssim 0.1 \varepsilon/k_B$. As temperature increases above $\simeq 0.1 \varepsilon/k_B$, the pressure becomes a decreasing function of temperature.

The pressure variation as a function of temperature at densities $\rho\sigma^3 \geq 0.3$ is universal, and, depending on the temperature range, three different regimes can be identified. As is evident in Fig. 2, in this range of densities, the pressure increases monotonically with temperature. However, the rate of increase at temperatures below $\simeq 0.05 \varepsilon/k_B$ differs considerably from those, observed at intermediate temperatures, and those close to $\simeq 0.20 \varepsilon/k_B$. Thus, at temperatures higher than $\simeq 0.07 \varepsilon/k_B$, the dependencies flatten out significantly. The decrease in negative pressure is due to two important factors. First, the micro-structural rearrangements are fully controlled by thermally activated processes. However, the average density is the factor, which affects collective motion and - in effect - shapes the pore topography. An increase in density suppresses the mobility of atoms at a fixed temperature. Correspondingly, at low temperatures, the relaxation is a strong function of temperature. In the intermediate range of temperatures, between $\simeq 0.05 \varepsilon/k_B$ and $0.15 \varepsilon/k_B$, the rates of pressure variation are smaller compared to the low-temperature range, yet a significant decrease in pressure magnitude is observed at all densities studied. At low densities, this regime corresponds to a nearly complete relaxation at any temperature (above $\simeq 0.15 \varepsilon/k_B$). As expected, in the third region, a nearly flat dependence is observed. Note that *qualitative features* of the topographical patterns do not change with temperature. Also, in the whole range of temperatures, the observed variations in pressure with temperature are rather small, as compared to the effects due to the average density. Indeed, the pressure changes by approximately an order of magnitude, while the average density varies in the range $\rho\sigma^3 \in [0.2, 0.9]$.

In order to establish a more quantitative basis for estimating the effect of density, in the inset to Fig. 2, we show the data collapse obtained by using the scaling relation $P/T \sim \rho^\alpha$ with $\alpha \simeq 5/2$. Given such a strong dependence, we conclude that pressure is largely controlled by the *average density* in a wide range of $\rho\sigma^3$. Also, pressure depends on topological properties of void domains. One of the possible explanation for such a behavior is that it is associated with surface energy. However, further studies of the near-surface effects should be performed to uncover all the details of the observed behavior. Note that the deviations from the scaling behavior are quite significant at $\rho\sigma^3 \leq 0.3$ and $\rho\sigma^3 = 0.9$.

B. Pore size distribution functions

Further analysis involves pore-size, d_p , distribution (PSD) functions, $\Phi(d_p)$. To quantify the topographical properties of the ensembles of pores (see Fig. 1 for illustration), we employed the methods and the computer code developed in Refs. [47, 48]. Fig. 3 shows the behavior of the PSD functions, computed at different values of $\rho\sigma^3$. As can be observed in Fig. 3, in the region of small pore-sizes, each PSD is an increasing function of d_p , for sizes below a characteristic length-scale. Note that both the rate of increase of the PSDs and their magnitudes are smallest at $\rho\sigma^3 = 0.2$. In general, both of these quantities are increasing functions of $\rho\sigma^3$. At larger d_p values, the PSDs flatten out. One more common feature of systems with $\rho\sigma^3 < 0.9$ is that they exhibit a peak at d_p values close to maximum pore-sizes. The above behavior is qualitatively different from that of dense systems. In this respect, the cases with $\rho\sigma^3 = 0.9$ and 1.0 are representative examples. Indeed, in dense systems, the PSDs profiles are close to Gaussian (see the orange dashed curve in Fig. 3). In this case; *i.e.*, the PSDs are fully described by the position of the peak and the width of the distribution. As shown below, there exists a universal scaling in the regime of small and intermediate length-scales. To formulate the corresponding scaling law, let us introduce the average pore diameter as: $\langle d \rangle = \sum_{i=1}^M d_{p(i)}^2 n_{d_{p(i)}} / \sum_{i=1}^M d_{p(i)} n_{d_{p(i)}}$, where $n_{d_{p(i)}}$ is the number of pores having discrete diameter $d_{p(i)}$ and M is the number of the discretization points [49]. Further, for the equilibrium continuous PSDs, $\Phi(d_p)$, we postulate the following scaling *ansatz*:

$$\Phi(d_p) \sim (d_p/\langle d \rangle)^\gamma f(d_p/\langle d \rangle). \quad (2)$$

The function $f(x)$ possess the following properties: a) $f(x \leq 1) \sim \text{const}$; b) $f(0.5 < x < 1.5) \sim x^{-\gamma}$. We applied the scaling form to the data obtained on all the considered herein systems. The scaling collapse for all $\rho\sigma^3$ is shown in the inset to Fig. 3. As can be observed in the figure, the data collapse is quite convincing. The following findings are noteworthy. First, there exists a universal exponent $\gamma \simeq 3$, which describes the data for all densities up to $\rho\sigma^3 = 0.8$ inclusive. Second, the average pore diameter is a strong function of porosity. By a numerical analysis of the corresponding quantities, we found the following relation between the average pore size and porosity: $\langle d \rangle \sim p^\delta$, where δ is close to 2/3, as shown in Fig. 3. In essence, this relation signifies the fact that the average pore size is determined by the average surface area of the void space inside the solid material. The maximum pore diameter, d_m , is defined by the effective size of the available free space, which can be approximated as

$\lambda = p^{1/3}L$, where L is the linear system size. The relation holds for all densities, such that $\rho\sigma^3 \leq 0.8$. Also, the deviation from the scaling law, Eq. (1), occurs at the length-scales close to d_m . This indicates the existence of two independent length-scales in the system: $\langle d \rangle$ and d_m . The effects associated with the second length-scale manifest itself by the observed deviations in the scaling behavior at $d_p/\langle d \rangle$ values above 1.5 [see the inset in Fig. 3].

The behavior of the PSDs was studied in a temperature interval between $0.02 \varepsilon/k_B$ and $0.20 \varepsilon/k_B$. We found that the general shape of the PSD functions is preserved in the whole range of temperature variation. At small pore diameters, all the PSD functions follow a power-law behavior, with the power-law exponent close to $\simeq 3.0$. Further, in the range of intermediate d_p values, $\Phi(d_p)$ flattens out. Thus, the scaling relation, Eq. (2), holds in the whole temperature range studied. Correspondingly, a variation in temperature changes only the width and height of the PSDs, leaving the other features intact. Note, however, that, in the proximity of the maximum pore diameter, d_m , a peak is observed. We found that the magnitude of the peak is nearly negligible, when temperature is less than $\simeq 0.05 \varepsilon/k_B$. At higher temperatures the peak magnitude increases, being $\simeq 100\%$ greater than that of the plateau region at $T = 0.2 \varepsilon/k_B$. As explained above, the PSD functions can be regarded as piecewise combinations of two distinctive part. The first part corresponds to small and intermediate pore diameters and is described by Eq. (2). The second part corresponds to a separate peak in the vicinity of d_m . In this regions, the scaling breaks down. Although, the general shape of the PSDs is not affected by the variation in temperature, the parameters of distributions vary substantially. The maximum pore diameter versus temperature is plotted in Fig. 4 at different values of $\rho\sigma^3$. As can be observed in the figure, at every $\rho\sigma^3$ value, d_m is an increasing function of temperature, as expected. Moreover, the relative maximum increments in d_m due to temperature variations are independent of $\rho\sigma^3$ and can roughly be estimated as $\simeq 30\%$. One curious feature of behavior is worth noting. Three density ranges can be discriminated in Fig. 4. In each density range, the curves show remarkably similar behavior in what related not only d_m values, but also the specifics of the functional dependence. From this behavior, one can infer that there exist dynamical constraints on the pore evolution, such that there is no continuous dependence of the pore-formation dynamics on density.

C. Local density distributions

In the preceding sections, we studied the properties of pores in the glassy systems. In what follows, the focus is put on the solid domains of the model systems under consideration. In particular, we compute local densities in the solid-phase domains. Henceforth, the local density is defined by a number of atoms located within a predefined radial range centered on a site of the cubic lattice $L \subset \mathbb{R}^3$. Correspondingly, for each lattice site, we define a closed ball, $B_R = \{R \in \mathbb{R}^3 : \sum_{j=1}^3 R_j^2 \leq R_0^2\}$, where $R_0 = |\vec{R}_0|$ is a fixed rational number. Then, the average density is given by: $\langle \rho \rangle = 1/V \sum_{i=1}^N \delta(\vec{r}_i) = N/V = \rho\sigma^3$. The on-site *local density* is computed as $\langle \rho \rangle_R = 1/B_R \int_{B_R} dR^3 \delta(\vec{r}_i - \vec{R})$, where the integral is taken over B_R . Note that the local density, $\langle \rho \rangle_R$, depends on R_0 . In our calculations, we used a fixed value of $R_0 = 2.5\sigma$. The rationale for choosing this value is based upon the behavior of $\langle \rho \rangle_R(R_0)$ in dense (nearly void-free) glasses. At this value of R_0 the local density becomes constant and thus is equal to the *average density* of a homogeneous non-porous glass. That is why, $\langle \rho \rangle_R$ can be regarded as *a measure of deviation of the local density from the average density* of homogeneous dense glass. In Fig. 5, we plot the local density distribution functions, $\Pi(\langle \rho \rangle_R)$, computed at nine different average densities. As can be seen in the figure, depending on $\rho\sigma^3$, three different types of behavior can be discriminated (see lower, middle, and upper panels of the figure). In the regime of small $\rho\sigma^3$ values (upper panel), the major characteristic features are the following: a) a strong peak in the vicinity of zero density; b) $\Pi(\langle \rho \rangle_R)$ is a decreasing function of $\langle \rho \rangle_R$. This is not an unexpected behavior for binodal systems with a large fraction of pores. Indeed, pores and thin solid domains contribute to the peak at zero and small value of $\langle \rho \rangle_R$. Note that the surface to volume ratio in glassy phases is rather large in this regime and therefore particles located in near-surface regions contribute significantly to the behavior at intermediate $\langle \rho \rangle_R$. The functional dependence with $\langle \rho \rangle_R$ resembles closely a continuous decay. Note, however, that there is a peak in the region slightly above $\langle \rho \rangle_R = 1.2$. The nature of the peak is discussed below.

Lets us now turn the attention to the opposite case of dense, nearly homogenous glass. The panels g), h) and i) in Fig. 5 correspond to the large $\rho\sigma^3$ values. The behavior is, in a sense, the opposite to the one, observed at small values of $\rho\sigma^3$. Indeed, the highest peak is expected to be at a value close to the average density of the solid phase. The plateau centered at approximately $\rho\sigma^3 = 0.6$ is due to the near-surface regions of the solid domains,

where the numbers of atoms is close to one half of the bulk. Once again, a peak at a value of $\langle\rho\rangle_R$ close to 1.2 is observed. In the region of small values of $\langle\rho\rangle_R$, only a small deviation from zero can be seen. Those are due to local fluctuations in free volumes that can be regarded as microstructural defects. The peak in the intermediate range of the local density are due to atoms in near-surface regions of pores of small sizes. At the intermediate values of $\langle\rho\rangle_R$, the patterns can be regarded as a superposition of the two cases, discussed in the above. The solid domains are represented by the peaks at the densities characteristic for large values of $\rho\sigma^3$. The peaks near zero decrease in magnitude with the average density, while, at intermediate values of $\langle\rho\rangle_R$, the behavior is characteristic for bimodal systems with a large surface-to-volume ratio.

The behavior of $\Pi(\langle\rho\rangle_R)$ functions in the regions close to the maximum density requires an additional analysis. Those regions correspond to the density of solid domains, away from the interfaces with the pores, and thus are of interest for several reasons. First, mechanical response properties of porous materials depend on density of the solid phase. Second, diffusivity (as mentioned above, it is highly suppressed in the glassy states) is generally a decreasing function of density [50]. Here, we focus on the behavior of the average density of solid domains as a function of porosity. To get a measure of the solid phase average density, we define the quantity denoted as $\langle\rho\rangle_S$, such that it provides an average over the density distributions in the region around the maxima corresponding to the solid phases (in Fig. 5, the average solid phase density corresponds to the peaks around $\langle\rho\rangle_R = 1.2$). To find the average we assume that the peaks in regions close to $\langle\rho\rangle_R = 1.2$ can be approximated as Gaussian forms. Then, the parameters of each Gaussian curve can be obtained from the corresponding numerical fits. The porosity, p , was computed using the methods and the computer code developed by the authors of Refs. [47, 48]. In Fig. 6, we plot $\langle\rho\rangle_S$, as a function of p . As follows from the figure, the solid-phase density of the porous systems does not differ much from that of the dense ones. In the wide porosity range studied, the maximum variation in the density is less than $\simeq 5\%$. The behavior of $\langle\rho\rangle_S$ with porosity, however, possess some noteworthy features. First, there is a rather abrupt change in $\langle\rho\rangle_S$ in the region of small values of p . Second, in the high porosity limit, $p \geq 0.6$, the density is a strongly increasing function of p . At the intermediate values of p , $\langle\rho\rangle_S$ demonstrates a moderate growth. This range spans p values from $\simeq 0.1$ to $\simeq 0.5$. Next, we discuss the behavior of porosity with the average density, $\rho\sigma^3$. The result is shown in the inset to Fig.

6. As our analysis shows, the behavior can be represented by the following scaling relation $p \propto (\rho_c \sigma^3 - \rho \sigma^3)^\gamma$. In this formula, $\rho_c \sigma^3$ is the critical density, corresponding to $p = 0$. Curiously enough, the value, obtained from the fitting is: $\rho_c \sigma^3 = 1.24$. Note that the value $\rho_c \sigma^3 = 1.25$ was reported in Ref. [46] as the critical density below which LJ systems develop voids upon isochoric energy minimization. The computed power-law exponent is $\gamma \simeq 2.0$. The above relation works well at both the small and the intermediate values of $\rho \sigma^3$. At the values of $\rho \sigma^3$ greater than $\simeq 0.8$, deviations from the scaling behavior occur. Note that, in this region, $\langle \rho \rangle_R$ is a strongly increasing function of p . This means that the density changes drastically with a minor variation of p . The behavior is consistent with the large negative pressures at this value of $\rho \sigma^3$.

IV. CONCLUSIONS

In this paper, we studied the structural and thermodynamic properties of model glassy systems with varied porosity, obtained by an isochoric rapid quench from a liquid phase to low-temperature solid phases. The transition to vitreous phase occurs as an instability, defined by negative derivatives of the chemical potential and pressure with respect to the concentration and the local density, respectively. The equilibrium temperature of the glassy phases was varied in a relatively wide range to reveal effects of temperature on the thermodynamical properties and structural specifics of the porosity patterns. We computed the temperature dependence of the pressure in the systems with different densities and deduced a scaling law governing the behavior of the pressure-temperature with average densities. Further, the pore-size distribution functions were studied. We found that in the systems with porosity exceeding a characteristic value, the distribution function obey a single scaling relation. For the highly dense systems, the distribution resembles closely a Gaussian; this finding being in agreement with available experimental data. It was found that a change in temperature of the solid phase does not alter general shape of the pore-size distribution functions, the major effect being a widening of the curves. The local density distribution functions for samples with varied density were also scrutinized. We found that local density of the solid phase is a decreasing function of the porosity in the high porosity limit, while it decreases with the porosity for dense systems. The present study can be of use for design of porous absorbent materials and related technologies. Also, it can provide some insight into

mechanism of glass transition and structural defects in vitreous systems.

V. ACKNOWLEDGEMENT

The authors are indebted to Prof. M. Paluch (Institute of Physics, University of Silesia) for illuminating comments on the experimental aspects of the studies of glass transition in confined environments. Financial support from the NSF (CNS-1531923) is gratefully acknowledged. Computational work in support of this research was performed at Michigan State University's High Performance Computing Facility and the Ohio Supercomputer Center.

-
- [1] C. A. Angell, *Science* **267**, 1924 (1995); C. A. Angell, K. L. Ngai, G. B. McKenna, P. F. McMillan, and S. W. Martin, *J. Appl. Phys.* **88**, 3113 (2000).
 - [2] I. S. Gutzow and J. W. P. Schmelzer, *The Vitreous State: Thermodynamics, Structure, Rheology, and Crystallization*, 2nd ed. (Springer, Berlin, 2013).
 - [3] W. Kauzmann, *Chem. Rev.* **43**, 219 (1948).
 - [4] P. W. Anderson, in: *Ill-Condensed Matter: Les Houches Session XXXI*, Eds. R. Balain, R. Maynard, and G. Toulouse (North-Holland, Amsterdam), Course 3, pp. 162-258, 1978.
 - [5] P. G. Debenedetti and F. H. Stillinger, *Nature* **410**, 259 (2001).
 - [6] W. Kob and H. C. Andersen, *Phys. Rev. Lett.* **73**, 1376 (1994).
 - [7] S. Sastry, P. G. Debenedetti, and F. H. Stillinger, *Nature* **393**, 554 (1998).
 - [8] L. Angelani, R. Di Leonardo, G. Ruocco, A. Scala, and F. Sciortino, *Phys. Rev. Lett.* **85**, 5356 (2000).
 - [9] J. Broderix, K. K. Bhattacharya, A. Cavagna, A. Zippelius, and I. Giardina, *Phys. Rev. Lett.* **85**, 5360 (2000).
 - [10] C. Donati, F. Sciortino, and P. Tartaglia, *Phys. Rev. Lett.* **85**, 1464 (2000).
 - [11] B. Doliwa and A. Heuer, *Phys. Rev. Lett.* **91**, 235501 (2003).
 - [12] L. Berthier, *Phys. Rev. E* **69**, 020201 (2004).
 - [13] S. P. Whitlam, L. Berthier, and J. P. Garrahan, *Phys. Rev. Lett.* **92**, 185705 (2004).
 - [14] M. D. Ediger, *Ann. Rev. Phys. Chem.* **51**, 99 (2000).

- [15] L. Berthier and G. Biroli, *Rev. Mod. Phys.* **83**, 587 (2011).
- [16] T. G. Fox, Jr. and P. J. Flory, *J. Appl. Phys.* **21**, 581 (1950).
- [17] A. K. Doolittle, *J. Appl. Phys.* **22**, 1471 (1951).
- [18] D. Turnbull and M. H. Cohen, *J. Chem. Phys.* **34**, 120 (1961).
- [19] M. Hillert, *Acta Met.* **9**, 525 (1961).
- [20] J. W. Cahn, *Acta Met.* **10**, 179 (1962).
- [21] M. Laradji, O. G. Mouritsen, and S. Toxvaerd, *Phys. Rev. E* **53**, 3673 (1996).
- [22] S. K. Das, J. Horbach, and K. Binder, *J. Chem. Phys.* **119**, 1547 (2003).
- [23] S. K. Das, S. Puri, J. Horbach, and K. Binder, *Phys. Rev. E* **73**, 031604 (2006).
- [24] P. C. Hohenberg and B. I. Halperin, *Rev. Mod. Phys.* **49**, 435 (1977).
- [25] D. Gunton, M. San Miguel, and P. S. Sahni, in: *Phase Transitions and Critical Phenomena*, eds. C. Domb and J. L. Lebowitz, Vol. 8, p. 267 (Academic, New York, 1983).
- [26] K. Binder, *Phys. Rev. A* **219**, 341 (1984).
- [27] M. A. Makeev, M. A. Mazo, and E. F. Oleynik, in: *Physical and Chemical Methods of Study of Structure and Dynamics of Molecular Systems*, Proceedings of the All-Russian Conference, June 27-July 2, Yoshkar-Ola, Russia, 1994, Vol. 2, pp. 41-44 (in Russian).
- [28] L. Yang, D. J. Srolovitz, and A. F. Yee, *J. Chem. Phys.* **110**, 7058 (1999).
- [29] D. Sappelt and J. Jackle, *Europhys. Lett.* **37**, 13 (1997).
- [30] V. Testard, L. Berthier, and W. Kob, *Phys. Rev. Lett.* **106**, 125702 (2011).
- [31] V. Testard, L. Berthier, and W. Kob, *J. Chem. Phys.* **140**, 164502 (2014).
- [32] P. Pissis, D. Daoukaki-Diamanti, L. Apekis, and C. Christodoulides, *J. Phys.: Condens. Matter* **6**, L325 (1994).
- [33] J.-Y. Park and G. B. McKenna, *Phys. Rev. B* **61**, 6667 (2000).
- [34] C. L. Jackson and G. B. McKenna, *J. Non-Cryst. Solids* **131-133**, 221 (1991).
- [35] J. A. Forrest, K. Dalnoki-Veress, J. R. Stevens, and J. R. Dutcher, *Phys. Rev. Lett.* **77**, 2002 (1996).
- [36] C. L. Jackson and G. B. McKenna, *Chem. Mater.* **8**, 2128 (1996).
- [37] S. Simon, J.-Y. Park, and G. McKenna, *Eur. Phys. J.* **E8**, 209 (2002).
- [38] K. Adrjanowicz, K. Kaminski, K. Koperwas, and M. Paluch, *Phys. Rev. Lett.* **115**, 265702 (2015).
- [39] M. Tarnacka, O. Madejczyk, K. Kaminski, and M. Paluch, *Macromolecules* **50**, 5188 (2017).

- [40] W. Kob and H. C. Andersen, *Phys. Rev. E* **48**, 4364 (1993).
- [41] S. Plimpton, *J. Comp. Phys.* **117**, 1 (1995).
- [42] A. R. Yavari, A. Le Moulec, and A. Inoue, N. Nishiyama, N. Lupu, E. Matsubara, W. J. Botta, G. Vaughan, M. Di Michiel, and A. Kvik, *Acta Mater.* **53**, 1611 (2005).
- [43] G. Dlubek, A. P. Clarke, H. M. Fretwell, S. B. Dugdale, and M. A. Alam, *Phys. Stat. Sol. (A)* **157**, 351 (1996).
- [44] S. P. Andersson and O. Andersson, *Macromolecules* **31**, 2999 (1998).
- [45] S. Sastry, D. S. Corti, P. G. Debenedetti, and F. H. Stillinger, *Phys. Rev. E* **56**, 5524 (1997);
S. Sastry, P. G. Debenedetti, and F. H. Stillinger, *Phys. Rev. E* **56**, 5533 (1997).
- [46] Z. Shi, P. G. Debenedetti, F. H. Stillinger, and P. Ginart, *J. Chem. Phys.* **135**, 084513 (2011).
- [47] R. L. Martin, B. Smit, and M. Haranczyk, *J. Chem. Inf. Model.* **52**, 308 (2012).
- [48] T. F. Willems, C. H. Rycroft, M. Kazi, J. C. Meza, and M. Haranczyk, *Micropor. Mesopor. Mater.* **149**, 134 (2012).
- [49] T. Nakayama, K. Yakubo, and R. L. Orbach, *Rev. Mod. Phys.* **66**, 381 (1994).
- [50] M. J. Nuevo, J. J. Morales, and D. M. Heyes, *Phys. Rev. E* **55**, 4217 (1997).

Figures

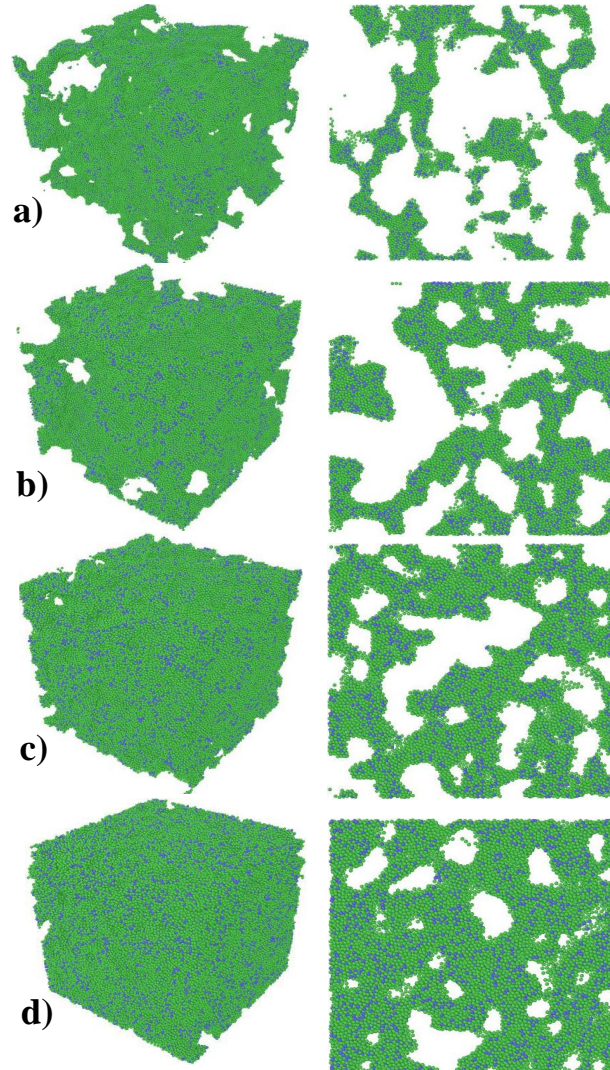


FIG. 1: (Color online) Equilibrium instantaneous atomic configurations of the glassy phases, computed at different values of $\rho\sigma^3$: a) 0.3, b) 0.5, c) 0.7, and d) 0.9 (from top to bottom). All the configurations are obtained at $T = 0.05 \varepsilon/k_B$. The left panels show the full three-dimensional plots of the atomic configurations and the right panels display slices of the central parts of the simulation cell with thickness of 5σ . Different colors mark atomic types A and B .

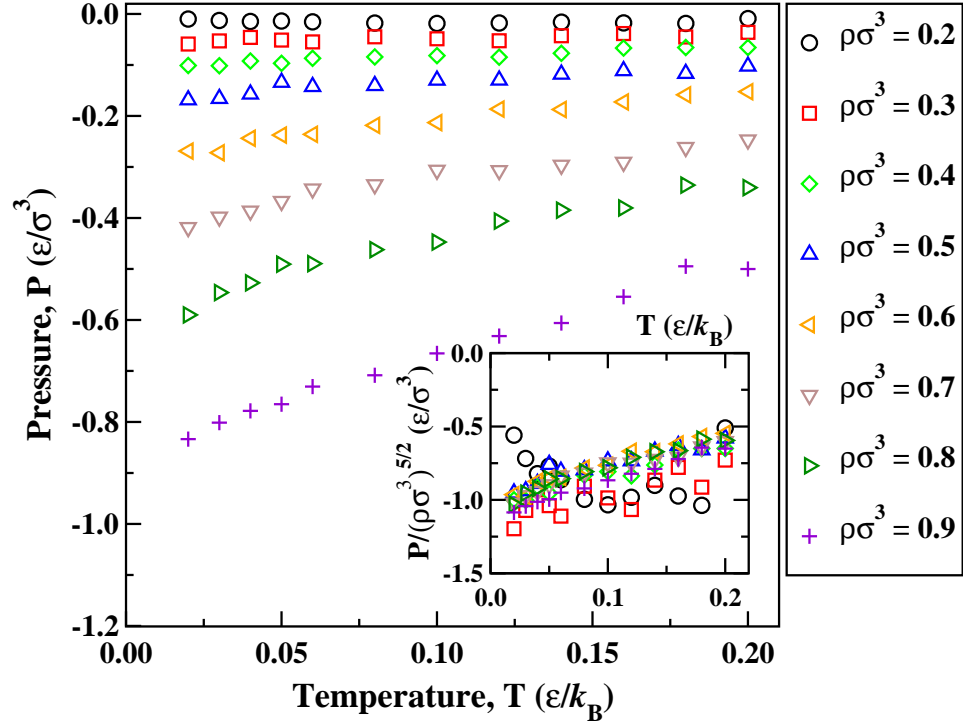


FIG. 2: (Color online) The average pressure, P , in equilibrium systems as a function of temperature, T , for the indicated values of $\rho\sigma^3$. The inset shows the scaling collapse using $P/T \sim \rho^\alpha$ relation. See text for details.

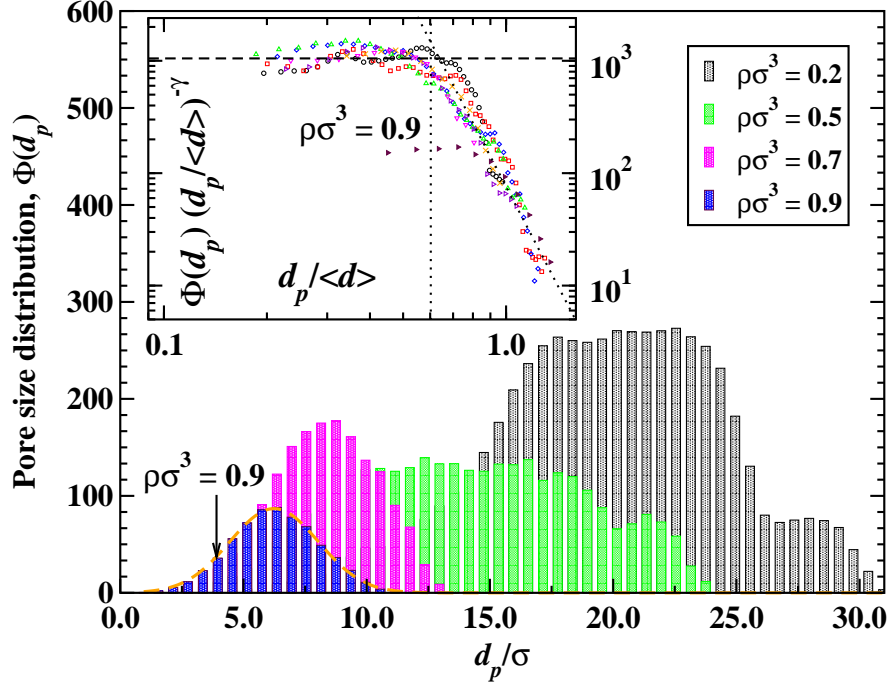


FIG. 3: (Color online) The pore size distribution functions, $\Phi(d_p)$, computed for systems with densities $\rho\sigma^3 \in \{0.2, 0.5, 0.7, 0.9\}$ and $T = 0.05 \varepsilon/k_B$. In the analysis, the original bin size is fixed at $\simeq 0.05 \sigma$. Subsequent averaging was performed within $\simeq 0.5 \sigma$; a reduced set of data points for each $\rho\sigma^3$ is shown for clarity. The dashed orange curve is a Gaussian fit to the $\rho\sigma^3 = 0.9$ data. The inset shows the data collapse for all densities according to Eq. (1). The same color code as in Fig. 3.

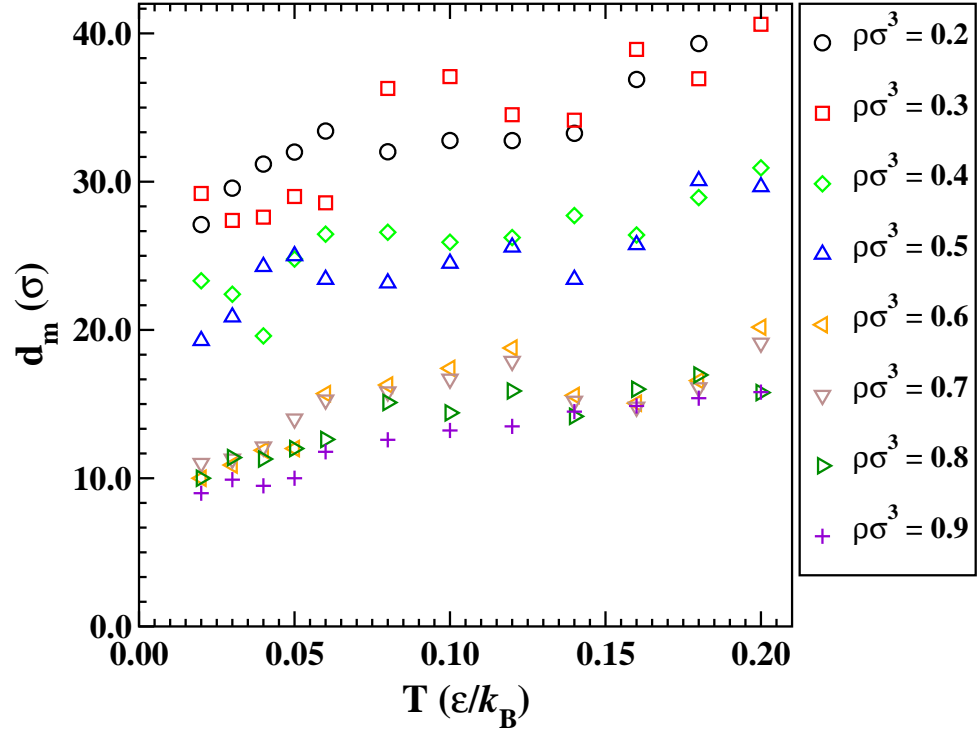


FIG. 4: (Color online) The maximum pore diameter, d_m , is plotted as a function of temperature for the tabulated values of $\rho\sigma^3$.

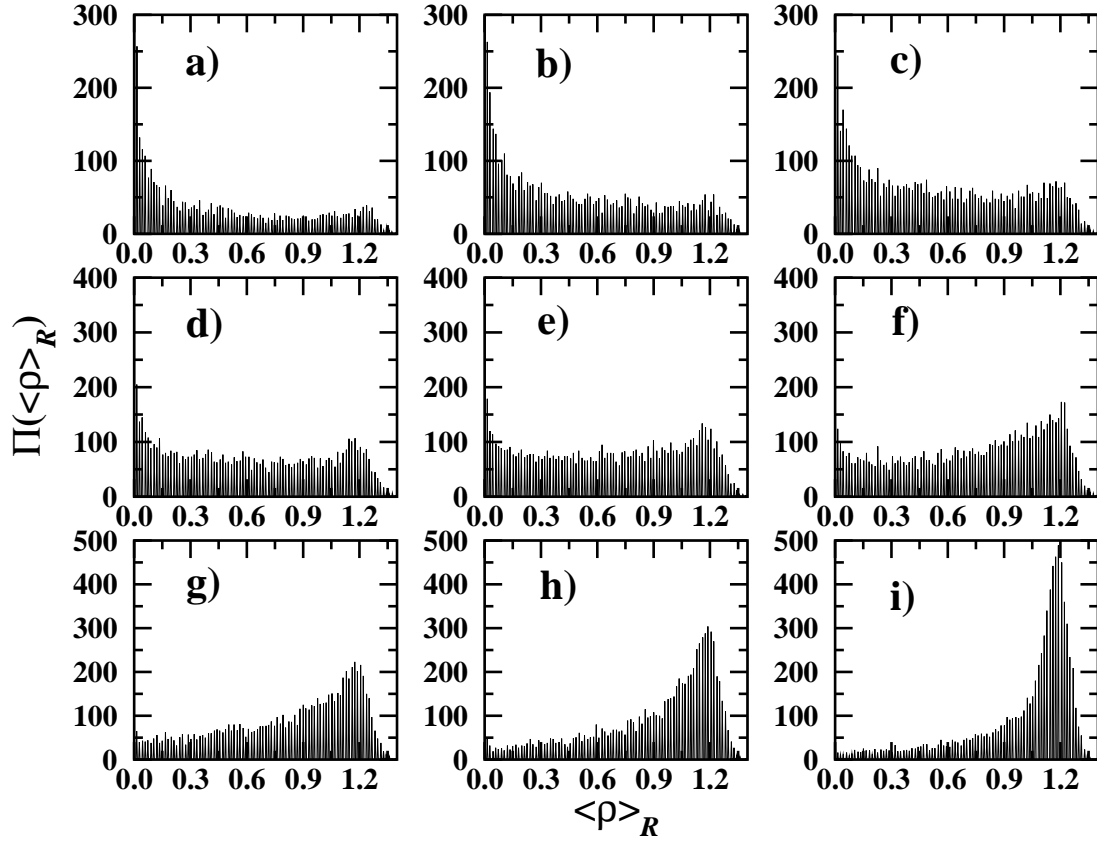


FIG. 5: On-lattice local density distribution functions, $\langle \rho \rangle_R$, are shown for the normalized average density, $\rho\sigma^3$, values: a) 0.2, b) 0.3, c) 0.4, d) 0.5, e) 0.6, f) 0.7, g) 0.8, h) 0.9, and i) 1.0. The distribution functions are computed using the bin size of $\langle \rho \rangle_R^{max}/400$ and $T = 0.05 \varepsilon/k_B$; no averaging of any kind is involved.

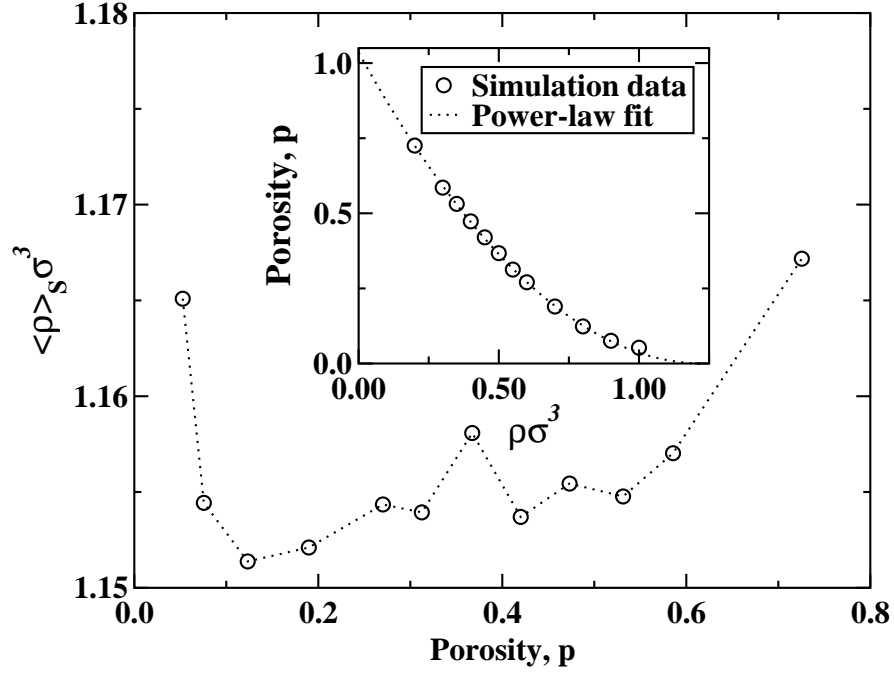


FIG. 6: Average density of solid-phase domains, $\langle \rho \rangle_S$, is plotted as a function of the porosity, p . The inset shows the porosity versus $\rho \sigma^3$ dependence (open circles). The power-law fit to the simulation data is indicated by the dashed curve. The fitting procedure is discussed in the text.